Q-Ball Images Segmentation Using Region-Based Statistical Surface Evolution

Maxime Descoteaux, Rachid Deriche

INSTITUT NATIONAL DE RECHERCHE EN INFORMATIQUE ET EN AUTOMATIQUE

Q-Ball Images Segmentation Using Region-Based Statistical Surface Evolution

Maxime Descoteaux — Rachid Deriche

N° 6257

August 2007

Thème BIO

ISSN 0249-6399

Q-Ball Images Segmentation Using Region-Based Statistical Surface Evolution

Maxime Descoteaux* , Rachid Deriche†

Thème BIO — Systèmes biologiques
Projet Odyssée

Rapport de recherche n° 6257 — August 2007 —25 pages

Abstract: In this article we develop a new method to segment Q-Ball imaging (QBI) data. We first estimate the orientation distribution function (ODF) using a fast and robust spherical harmonic (SH) method. Then, we use a region-based statistical surface evolution on this image of ODFs to efficiently find coherent white matter fiber bundles. We show that our method is appropriate to propagate through regions of fiber crossings and we show that our results outperform state-of-the-art diffusion tensor (DT) imaging segmentation methods, inherently limited by the DT model. Results obtained on synthetic data, on a biological phantom, on real datasets and on all 13 subjects of a public QBI database show that our method is reproducible, automatic and brings a strong added value to diffusion MRI segmentation.

Key-words: diffusion tensor imaging (DTI), high angular resolution diffusion imaging (HARDI), Q-ball imaging (QBI), orientation distribution function (ODF), region-based segmentation, level set framework, Riemannian and Euclidean distances

* Maxime.Descoteaux@sophia.inria.fr
† Rachid.Deriche@sophia.inria.fr

Évolution de Surface par Statistique de Région pour la Segmentation en Imagerie par Q-Ball

Résumé : Nous proposons une méthode de segmentation des images de diffusion à haute résolution angulaire (HARDI) obtenues en imagerie par Q-ball (QBI). D'abord, la fonction de distribution d'orientation (ODF) des fibres de la matrière blanche est estimée à l'aide de la base des harmoniques sphériques et d'une méthode d'estimation récente, analytique, robuste et rapide. Ensuite, nous utilisons une évolution de surface par statistique de région sur cette image d'ODF pour retrouver des ensembles de faisceaux de fibres cohérents partageant les mêmes caractéristiques. Nous montrons que notre nouvelle méthode reproduit les résultats état de l'art basés sur le tenseur de diffusion (DT) et que nous améliorons les résultats de segmentation dans les régions de croisements de faisceaux fibres, là où le DT est intrinsèquement limité. Enfin, nos résultats sur des données simulées, sur un fantôme biologique, sur des données réelles ainsi que sur la base de données HARDI publique comportant 13 sujets démontrent que notre approche est reproductible, automatique et apporte une valeur ajoutée importante pour la segmentation d'images IRM pondérées en diffusion.

Mots-clés : Imagerie du tenseur de diffusion (DTI), imagerie de diffusion à haute résolution angulaire (HARDI), imagerie par Q-ball (QBI), function de distribution des orientations (ODF), segmentation, courbe de niveau, distances Riemannienne et Euclidienne

Contents

1 Introduction

We would like to segment white matter fiber bundles in which diffusion properties are similar and ultimately compare their features to those in other ROI in the same subject or on multiple subjects. The goal is thus to find global coherence that exist among white matter fiber tracts belonging to the same fiber bundle. Existing DTI-based segmentation techniques [16, 24, 32, 38, 40, 42] are inherently limited by the DT model and most often blocked in regions of fiber crossings where DTs are oblate and isotropic. This is why recent high angular resolution diffusion imaging (HARDI) techniques such as QBI [34] have been proposed to aid the inference of crossing, branching and kissing fiber configurations. New methods have thus started to appear to segment bundles from fields of ODFs [23, 25].

In this paper, we answer the following three questions: 1) How can the segmentation problem be formulated and solved efficiently on a field of ODFs? 2) What is gained by the ODF with respect to the DT? 3) Is it possible to validate the segmentation results and make the segmentation automatic? To do so, we propose an efficient region-based level set approach using a regularized and robust spherical harmonics (SH) representation of the ODF [15]. We first show that a better local modeling of fiber crossings improves segmentation results globally. Then, we show that our ODF segmentation is more accurate than the state-of-the-art DTI segmentation based on the Euclidean and Riemannian distances [24] in regions of complex fiber configurations from synthetic data, from a biological phantom and from real data. The ODF better captures statistics in crossing areas and is thus able to flow through complex fiber regions without leaking in the whole white matter. Finally, we show that our Q-ball segmentation is reproducible by segmenting automatically the corpus callosum (CC) and the cortico spinal tract (CST) of the 13 subjects of a public QBI database [30].

The paper is organized as follows. Section 2 reviews the existing algorithms for segmentation of white matter fiber bundles from diffusion MRI data. Section 3.1 describes our regularized, fast and robust analytical ODF reconstruction for QBI [15]. Section 3.2 presents our ODF statistical surface evolution implemented using the level set framework. Then, results comparing state-of-the-art DTI segmentation [24] and our automatic ODF segmentation are presented in Section 4 on synthetic datasets and a biological phantom with known ground truth and on real datasets from the database [30]. Finally, we conclude with a discussion of the results and present directions for future work in Sections 4 and 5.

2 Background on Segmentation of White Matter Fiber Bundles

DT-based Segmentation The existing DT-based segmentation techniques in the literature are [16, 24, 32, 38, 40, 42]. In [42] they define an invariant anisotropy measure in order to drive the evolution of a level set and isolate strongly anisotropic or strongly isotropic regions on the brain, such as the CC and the ventricles. However, the reduction of the full tensor to a single scalar value can result in a relatively low discriminate capability and potentially yields the segmentation of mixed structures. Alternatively, [16, 22, 24, 32, 37, 38, 40] use or propose different measures of dissimilarity between DTs. In [24, 32, 38, 40], the authors use the the Euclidean distance to compare DTs. In [40], a k-means algorithm is used with a spatial coherence constraint and in [37], an active contour model

with a regularity term is used to perform the segmentation of different cerebral structures such as the thalamus nuclei and the CC. In [38], a generalization of the region-based active contours to matrix-valued images is proposed. However, it is restricted to the two-dimensional (2D) case and obviously limited when it comes to 3D brain data. In [16], partial differential equations based on mean curvature motion, self-snakes and geodesic active contour models are extended to 2D and 3D tensor-valued images by generalizing the notion of structure tensor to matrix-valued data. This method also relies on the Euclidean metric between DTs. In [22], the authors introduce a geometric measure of dissimilarity by computing the normalized tensor scalar product of two tensors, which can be interpreted as a measure of overlap. Finally, the methods exposed in [38] and [24] rely on the symmetrized Kullback-Leibler divergence and Riemannian geodesic metric to derive an affine invariant dissimilarity measure between DTs. In this paper, our statistical surface evolution using level sets is inspired by the original method of [29] and recent DTI extension of [24, 32], where a similar region-based surface propagation is implemented also using the level set framework.

HARDI-based Segmentation To our knowledge there are only two existing HARDI-based segmentation algorithms [23, 25]. In [23], the segmentation is developed in a non-Euclidean 5 dimensional (5D) position-orientation space, $(x, y, z, \theta, \phi) \in \Re^3$ x $\mathbf{S}^2$. using the ODF map reconstructed from diffusion spectrum imaging (DSI) [7, 39], a procedure computationally more expensive than QBI. The extension from 3D to 5D space leads to work with huge 5D matrices and there are important problems with data handling and storage, which only allows to segment small parts of cerebral structures. In [25], the main contribution is to model the ODF with a mixture of von Mishes-Fisher distributions and use the associated metric in a hidden Markov measure field segmentation scheme. Both the ODF modeling and the segmentation technique are different from our proposed method. Overall, for both segmentation algorithms [23, 25], the experimental and validation parts are different.

In this paper, we propose an efficient level set statistical surface evolution based on the ODFs computed from QBI that we thoroughly test on synthetic and real data with complex fiber configurations. The level set implementation is simple and efficient and the statistical evolution is robust with automatic convergence. Moreover, the ODF reconstruction from QBI has several advantages that make it a good choice of input image. First, samples are only taken on a single sphere in Q-space and thus, the imaging time is much smaller than that of the DSI despite significantly higher angular resolution measurements and good signal to noise ratio. Next, QBI also has the advantage of being model-independent which is not the case for other HARDI reconstruction methods such as the multi-fiber Gaussian models [35], spherical deconvolution approaches [2, 33] or the diffusion orientation transform (DOT) [28] where a fiber response function needs to be assumed a priori. Finally, as we will see in the next section, the ODF can be reconstructed rapidly in a regularized and compact representation [15].

3 Methods

Given a HARDI signal with N discrete measurements on the sphere, we transform it into a spherical harmonic (SH) series of order ℓ with R coefficients ($R << N$) describing the diffusion ODF.

We first summarize the important contributions of our regularized, fast and robust analytical ODF reconstruction for QBI [15]. Then, we look for the most probable partition of this ODF image of SHs using our new region-based statistical surface evolution.

3.1 ODF Estimation from QBI

QBI [34] reconstructs the diffusion ODF directly from the N HARDI measurements on a single sphere. The ODF is intuitive because it has its maximum(a) aligned with the underlying population of fiber(s). However, computing statistics on a large number of discrete ODF values on the sphere is computationally heavy and infeasible to integrate into a segmentation algorithm of the whole brain. A more compact representation of the ODF is thus needed. In [3, 15, 19] a simple analytic spherical harmonic (SH) reconstruction of the ODF is proposed. For completeness of the article, we now review and develop the main parts of our regularized analytical ODF reconstruction solution. The idea is to first estimate HARDI signal on the sphere with a regularized spherical harmonics approximation and then do a simple linear transformation of the harmonics to obtain the desired regularized ODF.

Spherical Harmonic (SH) Estimation of the HARDI Signal The SH, normally indicated by Y_ℓ^m (ℓ denotes the order and m the phase factor), are a basis for complex functions on the unit sphere. Explicitly, they are given as follows

$$Y_\ell^m(\theta,\phi) = \sqrt{\frac{2\ell+1}{4\pi}\frac{(\ell-m)!}{(\ell+m)!}} P_\ell^m(\cos\theta) e^{im\phi} \tag{1}$$

where (θ,ϕ) obey physics convention ($\theta \in [0,\pi], \phi \in [0,2\pi]$) and P_ℓ^m is an associated Legendre polynomial. For $k = 0, 2, 4, \ldots, \ell$ and $m = -k, \ldots, 0, \ldots, k$, we define the new index $j := j(k,m) = (k^2+k+2)/2 + m$ and define our modified basis $\mathbf{Y}$ with elements Y_j such that

$$Y_j = \begin{cases} \sqrt{2}\cdot \text{Re}(Y_k^m), & \text{if } -k \le m < 0 \\ Y_k^0, & \text{if } m = 0 \\ \sqrt{2}\cdot \text{Img}(Y_k^m), & \text{if } 0 < m \le k \end{cases}, \tag{2}$$

where Re(Y_ℓ^m) and Img(Y_ℓ^m) represent the real and imaginary parts of Y_ℓ^m respectively. The basis is designed to be symmetric, real and orthonormal. Symmetry is ensured by choosing only even order SH and the ratios in front of each term also ensure that the modified basis is real and orthonormal with respect to the inner product $< f, g >= \int_\sigma f^* g d\sigma$, where σ denotes integration over the unit sphere and f^* is the complex conjugate of f, for f, g complex functions on the sphere. We thus approximate the signal at each of the N gradient directions i as

$$S(\theta_i,\phi_i) = \sum_{j=1}^{R} c_j Y_j(\theta_i,\phi_i) \tag{3}$$

where $R = (\ell+1)(\ell+2)/2$ is the number of terms in the modified SH basis $\mathbf{Y}$ of order ℓ. Letting $\mathbf{S}$ be the N x 1 vector representing the input signal for every encoding gradient direction, $\mathbf{C}$ the R x

1 vector of SH coefficients c_j and $\mathbf{B}$ is the NxR matrix constructed with the discrete modified SH basis

$$\mathbf{B} = \begin{pmatrix} Y_1(\theta_1,\phi_1) & Y_2(\theta_1,\phi_1) & \cdots & Y_R(\theta_1,\phi_1) \\ \vdots & \vdots & \ddots & \vdots \\ Y_1(\theta_N,\phi_N) & Y_2(\theta_N,\phi_N) & \cdots & Y_R(\theta_N,\phi_N) \end{pmatrix}, \tag{4}$$

we can write the set of equations as an over-determined linear system $\mathbf{S} = \mathbf{BC}$. We want to solve for the SH series coefficients c_j, where $c_j = \int_\sigma S(\theta,\phi)Y_j(\theta,\phi)d\sigma$.

At this point, instead of simply evaluating the integrals directly as done in [17] or performing a straightforward least-squared minimization as in [1, 33], we add local regularization directly into our fitting procedure. This is to be able to use a high order estimation without over-modeling the small perturbations due to noise in the input diffusion MRI signal. We thus define a measure, E, of the deviation from smoothness of a function f defined on the unit sphere as $E(f) = \int_\sigma (\triangle_b f)^2 d\sigma$, where $\triangle_b$ is the Laplace-Beltrami operator. Using the orthonormality of the modified SH basis, where we have $\int_\sigma Y_i(\sigma)Y_j(\sigma)d\sigma = \delta_{ij}$, the above functional E can be rewritten straightforwardly [15] as

$$E(f) \quad = \quad \int_\sigma \triangle_b \left(\sum_p c_p Y_p\right) \triangle_b \left(\sum_q c_q Y_q\right) d\sigma = \sum_{j=1}^{R} c_j^2 \ell(j)^2(\ell(j)+1)^2 = \mathbf{C}^{\mathrm{T}}\mathbf{L}\mathbf{C}, \tag{5}$$

where $\mathbf{L}$ is simply the R x R matrix with entries $\ell(j)^2(\ell(j)+1)^2$ along the diagonal ($\ell(j)$ is the order associated with the j^{th} coefficient, i.e for $j = 1,2,3,4,5,6,7,...$ $\ell(j) = 0,2,2,2,2,2,4,...$). We thus obtain a closed-form expression for the regularization term. Therefore, the quantity we wish to minimize can be expressed in matrix form as

$$M(\mathbf{C}) = (\mathbf{S}-\mathbf{BC})^{\mathrm{T}}(\mathbf{S}-\mathbf{BC}) + \lambda \mathbf{C}^{\mathrm{T}}\mathbf{L}\mathbf{C}, \tag{6}$$

where λ is the weight on the regularization term. The coefficient vector minimizing this expression can then be determined just as in the standard least-squares fit ($\lambda = 0$), from which we obtain the generalized expression for the desired spherical harmonic series coefficient vector

$$\mathbf{C} = (\mathbf{B}^{\mathrm{T}}\mathbf{B} + \lambda\mathbf{L})^{-1}\mathbf{B}^{\mathrm{T}}\mathbf{S}. \tag{7}$$

From this SH coefficient vector we can recover the signal on the Q-ball for any (θ,ϕ) as $S(\theta,\phi) = \sum_{j=1}^{R} c_j Y_j(\theta,\phi)$. Intuitively, this approach penalizes an approximation function for having higher order terms in its modified SH series. This eliminates most of the high order terms due to noise while leaving those that are necessary to describe the underlying function. However, obtaining this balance depends on choosing a good value for the parameter λ. We use the *L-curve* numerical method [18] and experimental simulations to determine a good smoothing parameter [14, 15]. Here, $\lambda = 0.006$ is used, as in [14, 15].

Analytic ODF Estimation The true diffusion orientation distribution function (ODF) in a unit direction $\mathbf{u}$, $\Psi(\mathbf{u})$, is given by the radial projection of the probability distribution function (PDF) of the diffusing water molecule. Tuch [34] showed that this diffusion ODF could be estimated directly

from the raw HARDI signal $\mathbf{S}$ on a single sphere of Q-space by the Funk-Radon transform (FRT). This FRT is essentially a smoothed version of the true ODF [34]. In practice, the FRT value at a given spherical point $\mathbf{u}$ is the great circle integral of the signal on the sphere defined by the plane through the origin with normal vector $\mathbf{u}$. In Appendix A, we show how this FRT can be evaluated analytically with an elegant corollary to the Funk-Hecke theorem [4]. The final ODF reconstruction on the sphere then becomes a simple linear transformation of the SH coefficients c_j describing the input HARDI signal $\mathbf{S}$,

$$\Psi(\theta,\phi) = \sum_{j=1}^{R} \underbrace{2\pi P_{\ell(j)}(0) c_j}_{f_j} Y_j(\theta,\phi), \tag{8}$$

where f_j are the SH coefficients describing the ODF Ψ and $P_{\ell(j)}(0) = (-1)^{\ell/2} \frac{1\cdot 3\cdot 5\cdots(\ell(j)-1)}{2\cdot 4\cdot 6\cdots\ell(j)}$ because $\ell(j)$ is always even in our modified SH basis. We see that the SHs are eigenfunctions of the Funk-Radon transform with eigenvalues depending only on the order ℓ of the SH series.

Hence, by using a SH estimation of the HARDI signal, we have showed that the QBI can be solved analytically. This was also showed in [3, 19]. An important contribution in favor of our approach is that this solution can be obtained while imposing a well-defined regularization criterion. The accuracy of the modified SH series approximation with the Laplace-Beltrami smoothing was established in [14] and our regularized ODF solution was also showed to have better fiber detection properties and showed to be more robust to noise than similar solutions [3, 19].

3.2 Statistical Surface Evolution

We now want to find a global coherence in this field of Q-ball ODFs represented in the SH basis. We denote the image of ODFs by $\mathcal{F} : \sigma \mapsto \Re^R$ so that for all $\mathbf{x} \in \sigma$, $\mathcal{F}(\mathbf{x})$ is an ODF of order ℓ represented by a vector of R real SH coefficients, $\mathcal{F}(\mathbf{x}) := \{f_1, ..., f_R\} \in \Re^R$. Now, the question is what is a good metric to compare ODFs?

Distances between ODFs We want to capture similarities and dissimilarities between two ODFs, i.e two spherical functions $\Psi, \Psi' \in \mathbf{S}^2$ that can be represented by real SH vectors $f, f' \in \Re^R$, as shown in the previous section. Since the ODFs come from real physical diffusion measurements they are bounded and form an open subset of the space of real-valued $\mathcal{L}^2$ spherical functions with an inner product $\langle , \rangle$ defined as

$$\langle \Psi, \Psi' \rangle = \int_{\mathbf{S^2}} \Psi(\sigma) \cdot \Psi(\sigma)' d\sigma = \int_{\mathbf{S^2}} \left(\sum_{i=1}^{R} f_i Y_i(\sigma) \sum_{j=1}^{R} f'_j Y_j(\sigma) \right) d\sigma. \tag{9}$$

As earlier, because of the orthonormality of the SH basis, the cross terms cancel and the expression is simply $\langle \Psi, \Psi' \rangle = \sum_{j=1}^{R} f_j \cdot f'_j$. Therefore, the induced $\mathcal{L}^2$ norm $||\Psi|| = \sqrt{\langle \Psi, \Psi' \rangle}$ giving us the

distance metric between two ODFs is

$$||\Psi - \Psi'|| = \sqrt{\sum_{j=1}^{R}(f_j - f'_j)^2}. \tag{10}$$

The Euclidean distance was also used successfully for DTI segmentation in [24, 32] even though more appropriate metrics exist such as the symmetrized Kullback-Leibler distance [24, 38] and Riemannian geodesic distance [24]. Similarly, one can think of choosing another metric to compare ODFs. For instance, since the ODF can be viewed as a probability distribution function (PDF) of fiber orientations, one can use the Kullback-Leibler distance between two PDFs, as done in [34]. However, in that case the problem quickly blows up computationally because one needs to use all N discrete data on the sphere instead of the R SH coefficients ($R << N$). For example, one needs to process $N = 200$ values instead of $R = 15$ SH coefficients.

Segmentation by Surface Evolution Inspired by general works on image segmentation [9, 29] , we search for the optimal partition $\mathcal{S}$ in two regions $\mathcal{S}_1$ and $\mathcal{S}_2$ of the image Ω. We maximize the *a posteriori* frame partition probability $p(\mathcal{S}|\mathcal{F})$ of obtaining the desired segmentation for the observed image of ODFs $\mathcal{F}$. The major difference in our approach is that we use order-4 ODFs, with $R = 15$ real coefficients whereas in the DT Euclidean flow of [24, 32], DTs represented by 6D vectors are used as input to the region-based segmentation. Note that the order-2 SH estimation of the ODF has six coefficients and is related to the DT [14, 27]. The Euclidean DTI segmentation [24, 32] is thus a special case of the ODF segmentation.

We use the level set framework [11, 12, 26] to represent the optimal partition $\mathcal{S}$ as the zero-crossing of the level set function ϕ. ϕ is defined as the usual signed distance function, i.e. $\phi(\mathbf{x}) = 0$ if $\mathbf{x} \in \mathcal{S}$, $\phi(\mathbf{x}) = \mathcal{D}(\mathbf{x}, \mathcal{S})$ if $\mathbf{x} \in \mathcal{S}_1$ and $\phi(\mathbf{x}) = -\mathcal{D}(\mathbf{x}, \mathcal{S})$ if $\mathbf{x} \in \mathcal{S}_2$, where $\mathcal{D}(\mathbf{x}, \mathcal{S})$ is the Euclidean distance between $\mathbf{x}$ and $\mathcal{S}$. Hence, the optimal partition is obtained by maximizing $p(\phi|\mathcal{F}) \propto p(\mathcal{F}|\phi)p(\phi)$ using Bayes rule. Assuming ODFs to be independent within each region, we have

$$p(\mathcal{F}|\phi) = \prod_{\mathbf{x}\in\mathcal{S}_1} p_1(\mathcal{F}(\mathbf{x})) \cdot \prod_{\mathbf{x}\in\mathcal{S}_2} p_2(\mathcal{F}(\mathbf{x})). \tag{11}$$

At this point, the main assumption is that p_1 and p_2 are Gaussians, which means that each SH coefficient of the ODFs follow a Gaussian distribution in the different partitions of the Q-ball image. Fig. 1 and Fig. 2 show that this Gaussian assumption is reasonable. In fact, we see that the histograms for most of the R coefficients of the ODF are "bell-shaped". Histograms were computed from all voxels in a manual segmentation of the CC and CST in a subject of the QBI database [30] (histograms are similar for all subjects of the database). Hence, we consider a parametric representation with a R-dimensional Gaussian. Letting $\overline{\mathcal{F}}_r \in \Re^R$ be the mean SH ODF vector in region $r = 1, 2$ and Λ_r be the R x R covariance matrix of the ODF vectors in region r, the likelihood of the ODF $\mathcal{F}(\mathbf{x})$ to be part of region r is defined as

$$p_r(\mathcal{F}(\mathbf{x})|\overline{\mathcal{F}}_r, \Lambda_r) = \frac{1}{(2\pi)^3|\Lambda_r|^{1/2}} \exp\left(-\frac{1}{2}(\mathcal{F}(\mathbf{x}) - \overline{\mathcal{F}}_r)^{\mathrm{T}}\Lambda_r^{-1}(\mathcal{F}(\mathbf{x}) - \overline{\mathcal{F}}_r)\right), \tag{12}$$

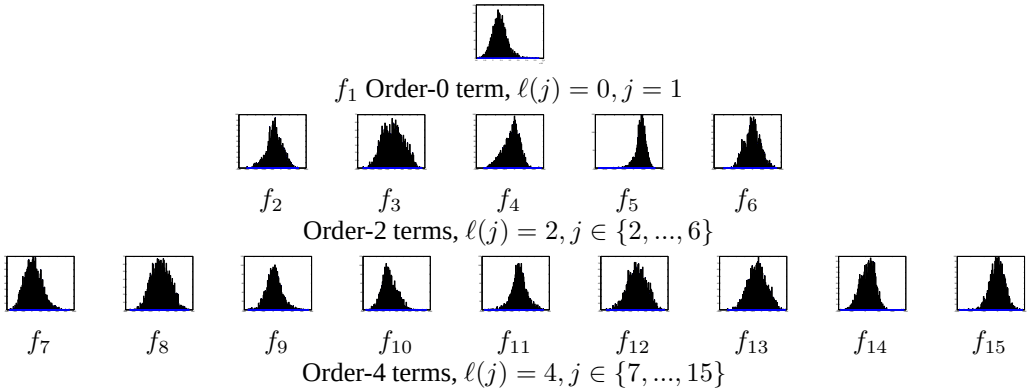

Figure 1: Histograms of the SH coefficients representation of the ODF $\{f_1, ..., f_{15}\}$ in the corpus callosum (CC). The CC was manually segmented from subject 7 of the public QBI database [30].

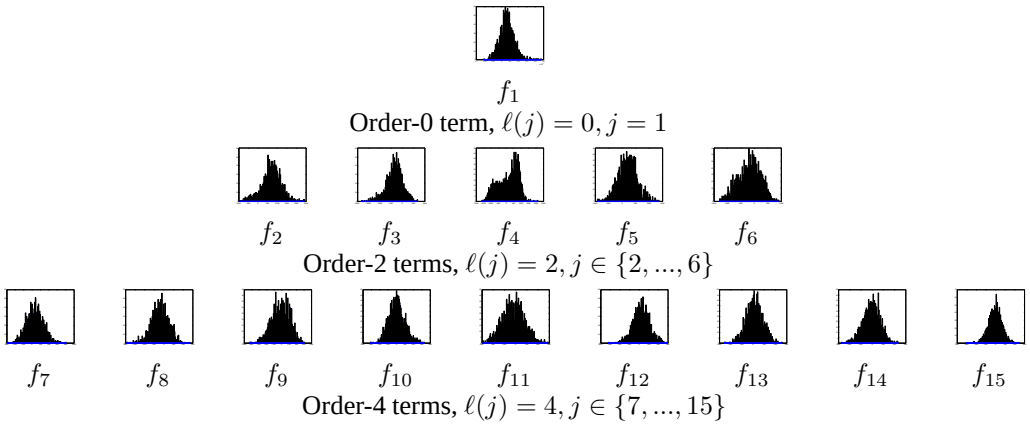

Figure 2: Histograms of the SH coefficients representation of the ODF $\{f_1, ..., f_{15}\}$ in the cortico spinal tract (CST). The CST was manually segmented from subject 7 of the public QBI database [30].

Concerning the term $p(\phi)$, it expresses the probability that the evolving surface represents the structure of interest and it can be used to introduce a prior shape knowledge [24]. Here, we want to favor structures with smaller surface $|\mathcal{S}|$ with $p(\phi) \propto \exp(-\nu|\mathcal{S}|)$. This can be expressed with ϕ by introducing the Dirac function [41] and thus, we have

$$p(\phi) = \exp(-\nu \int_{\Omega} \delta(\phi)|\nabla\phi(\mathbf{x})|d\mathbf{x}). \tag{13}$$

The optimal segmentation is then obtained by maximizing $p(\mathcal{F}|\phi)p(\phi)$ or by minimizing of the negative logarithms of Eqs. (12, 13) Therefore, the final energy minimization is

$$E(\phi, p_1, p_2) = -\int_{\Omega_1} \log p_1(\mathcal{F}(\mathbf{x})|\overline{\mathcal{F}}_1, \Lambda_1)d\mathbf{x} - \int_{\Omega_2} \log p_2(\mathcal{F}(\mathbf{x})|\overline{\mathcal{F}}_2, \Lambda_2)d\mathbf{x} + \nu \int_{\Omega} \delta(\phi)|\nabla\phi|d\mathbf{x}, \tag{14}$$

For given statistical parameters $\overline{\mathcal{F}}_1, \overline{\mathcal{F}}_2, \Lambda_1, \Lambda_2$ and regularization ν of the evolving surface, the Euler-Lagrange equation can be computed to derive the implicit surface evolution

$$\begin{aligned} \frac{\partial\phi}{\partial t} &= \delta(\phi)\left(\nu\,\mathrm{div}\frac{\nabla\phi}{|\nabla\phi|} + \log\frac{p_1(\mathcal{F}|\overline{\mathcal{F}_1}, \Lambda_1)}{p_2(\mathcal{F}|\overline{\mathcal{F}_2}, \Lambda_2)}\right) \\ &= \delta(\phi)\left(\nu\,\mathrm{div}\frac{\nabla\phi}{|\nabla\phi|} + \tfrac{1}{2}\left(\log\tfrac{|\Lambda_2|}{|\Lambda_1|} - (\mathcal{F}-\overline{\mathcal{F}}_1)^{\mathrm{T}}\Lambda_1^{-1}(\mathcal{F}-\overline{\mathcal{F}}_1) + (\mathcal{F}-\overline{\mathcal{F}}_2)^{\mathrm{T}}\Lambda_2^{-1}(\mathcal{F}-\overline{\mathcal{F}}_2)\right)\right). \end{aligned} \tag{15}$$

The statistics can be updated after each iteration of the ODF flow, as described in [24]. More details on this level set optimization can be found in [9, 10, 31, 36] The flow formulation is flexible and one can easily replace the input image vector of ODFs $\mathcal{F}$ with the standard DT coefficient vector, as in [24, 32]. We now compare the Euclidean DT [24, 32] version of the flow and more complex Riemannian DT [24] version of the flow with our proposed ODF flow.

3.3 Q-Ball Data Generation and Acquisitions

Synthetic Data We generate synthetic Q-ball data using the multi-tensor model [1, 14, 15, 19, 34],

$$S(\mathbf{u}_i) = \sum_{k=1}^{n} \frac{1}{n}\exp(-b\mathbf{u}_i^{\mathrm{T}}\mathbf{D}_{\mathbf{k}}(\theta)\mathbf{u}_i) + noise, \tag{16}$$

for N encoding directions $i \in \{1, ..., N\}$. We use $N = 81$ from a 3^{rd} order tessellation of the icosahedron, $b = 3000$ s/mm^2, $n = 1$ or 2 and $\mathbf{D}_{\mathbf{k}}(\theta)$ the diffusion tensor with standard eigenvalues $[300, 300, 1700]$x10^{-6} mm^2/s oriented in direction θ [15, 34]. The noise is generated with a complex Gaussian noise with a standard deviation of $1/35$, producing a signal with SNR 35.

We generate three synthetic data example, one with a 2-fiber 90° crossing (Fig. 3), another with a 2-fiber branching configuration (Fig. 5) and a last example (Fig. 6) simulating crossings that can occur between "U"-fibers (cortico-cortical fibers) and longer straight fiber bundles. These synthetic datasets help understand the behavior of the statistical surface evolutions when confronted with complex fiber geometries and different initializations. We compare the DT Riemannian [24] and ODF surface evolutions on this dataset and use $\nu = 2$ smoothness of the surface in the evolution.

Visualization In this paper, DTs and ODFs are visualized as spherical functions stretched with respect to the surface values. The surfaces are colored according to the Fractional Anisotropy (FA) [6], with colormap going from red to blue for anisotropic to isotropic diffusion profiles. We use this same colormap to allow easy visual comparisons between DTs and ODFs. As commonly done to accentuate ODF maxima, we min-max normalize [34] the ODFs before visualization.

Biological Phantom Data We obtained the biological phantom from Campbell et al [8]. It was created from two excised rat spinal cords embedded in 2% agar. The acquisition was done on 1.5T Sonata scanner using 90 encoding directions, with $b = 3000$ s/mm^2, TR$= 6.4$ s, TE$= 110$ ms, 2.8 mm isotropic voxels and four signal averages per direction. We compare the DT Euclidean [32], DT Riemannian [24] and ODF surface evolutions on this dataset and use $\nu = 2$ smoothness of the surface in the evolution.

Human Brain Data First, we use a human brain acquired at the Leipzig Max Planck Institute on a whole-body 3T scanner [5] with 60 encoding directions, with $b = 1000$ s/mm^2, 72 slices with 1.7mm thickness, twenty one $b = 0$ s/mm^2 images, 128 x 128 image matrix, TE $= 100$ ms, TR $= 12$ s. We compare the segmentations of the DT Euclidean [32], DT Riemannian [24] and ODF surface evolutions on two well-known fiber bundles, the corpus callosum (CC) and cortico spinal tract (CST). We use $\nu = 5$ smoothness of the surface in the evolution.

Then, we test our ODF segmentation on the public QBI database [30]. The 13 datasets were acquired on a 1.5T scanner with 200 encoding directions, $b = 3000$ s/mm^2, 60 slices with 2 mm thickness, twenty five $b = 0$ s/mm^2 images, 128 x 128 image matrix, TE $= 93.2$ ms, TR $= 1.9$ s. For each subject, a single voxel in the medial part of the CC and CST is selected (manually) to initialize the flow. We use $\nu = 10$ smoothness of the surface in the evolution.

4 Segmentation Results & Discussion

ODF-based segmentations can deal with regions of complex fiber configurations. We first show that the ODF flow is able to propagate through regions of complex fiber crossings better than the DT-based flow using the Euclidean and Riemannian distances [24, 32]. We show comparison results on synthetic data, on a biological phantom and on real datasets. We also show that the corpus callosum (CC) and the cortico-spinal tract (CST) of the QBI database [30] can be segmented automatically for all subjects and that there exist a variability in these structures across the subjects.

4.1 Synthetic Datasets

First, Fig. 3 shows that initialization has a strong influence on the final segmented surface. If the initialization contains strictly anisotropic DTs/ODFs, the final surface is not able to pass through the fiber crossing area, as seen in Fig. 3(a,b). Similarly, the final surface is trapped in the crossing area when initializing strictly in the 2-fiber region, as seen in Fig. 3(c). This is because the statistics of the initial region have a large difference with the rest of the DTs/ODFs and hence, the evolving surface is blocked from connecting to the rest of the structure. However, if the initialization contains a mixture of both single fiber and 2-fiber DTs/ODFs, the DT flow propagates through the crossing region to connect to the similar anisotropic DTs on the other side of the crossing and the second fiber is completely ignored, as seen in Fig. 3(d,e). The DTs in the crossing are oblate and there is no information on the second orientation. In contrary, there is information about the second orientation in the ODF flow and the surface evolution, seen in Fig. 4, finds the whole 2-fiber structure as coherent.

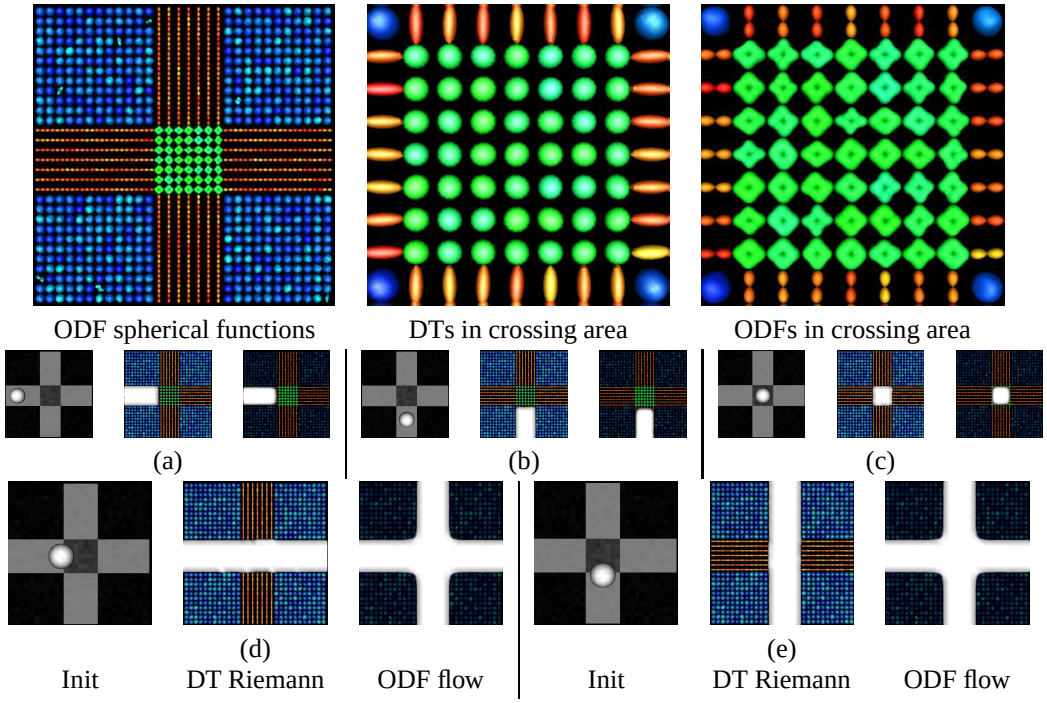

Figure 3: Segmentation of the 90° crossing example. In (a-e), from left to right, the initialization used overlaid on the FA map, the DT Riemannian [24] segmentation and the ODF flow segmentation.

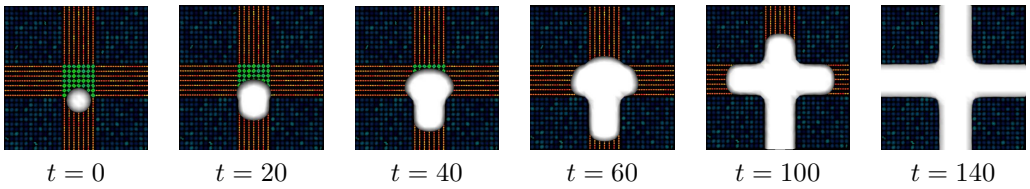

Figure 4: Evolution in time of the ODF flow on the 90° crossing. The flow is able to propagate through the fiber crossing area and recover the whole 2-fiber structure.

Fig. 5 and Fig. 6 show more complex fiber configurations with a branching example and the "U"-fibers example. In the Riemannian DT flow, we see that the surface remains trapped in the regions of the initial seeding for all initializations. In contrary, in the ODF case, when the flow is initialized in the bottom and middle part of the branch, the whole branching structure is recovered because the ODF contains a broader range of orientations in its statistics. For all synthetic data experiments,

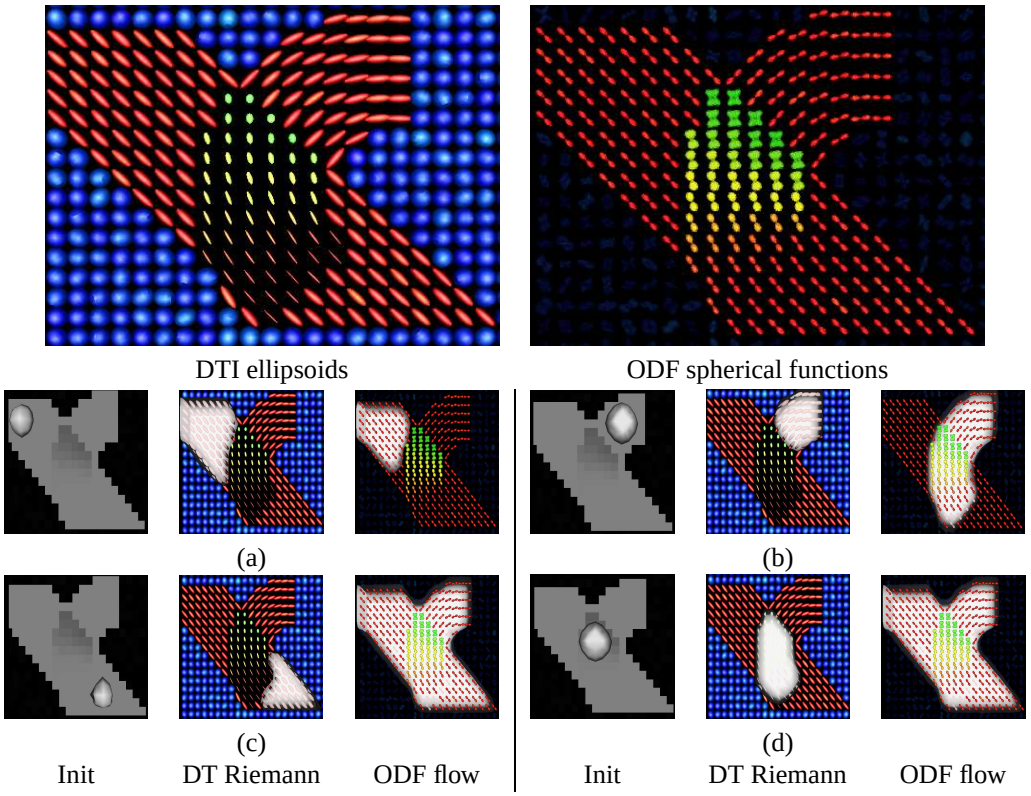

Figure 5: Segmentation on a synthetic branching example. In (a-d), from left to right, the initialization used overlaid on the FA map, the DT Riemannian [24] segmentation and the ODF flow segmentation. The ODF flow is able to propagate through the fiber crossing area and recover the whole structure.

DT Riemannian and DT Euclidean flows produced nearly identical qualitative segmentations and we decided only to show results for the DT Riemannian case.

4.2 Biological Phantom Dataset

Fig. 7 and Fig. 8 show that the DT flow with the Euclidean distance is unable to segment the structure. The surface leaks outside the cords and the surface diverges because the isotropic DTs in the fibers and isotropic DTs in the background have a mean diffusivity in a similar range. Hence, the Euclidean distance cannot make the difference between the two regions. This result was also obtained in [24]. However, our new ODF flow segments the whole structure quite easily. The segmentation also agrees with similar results published using the DT Riemannian flow [24, Fig.12-13]. This similarity

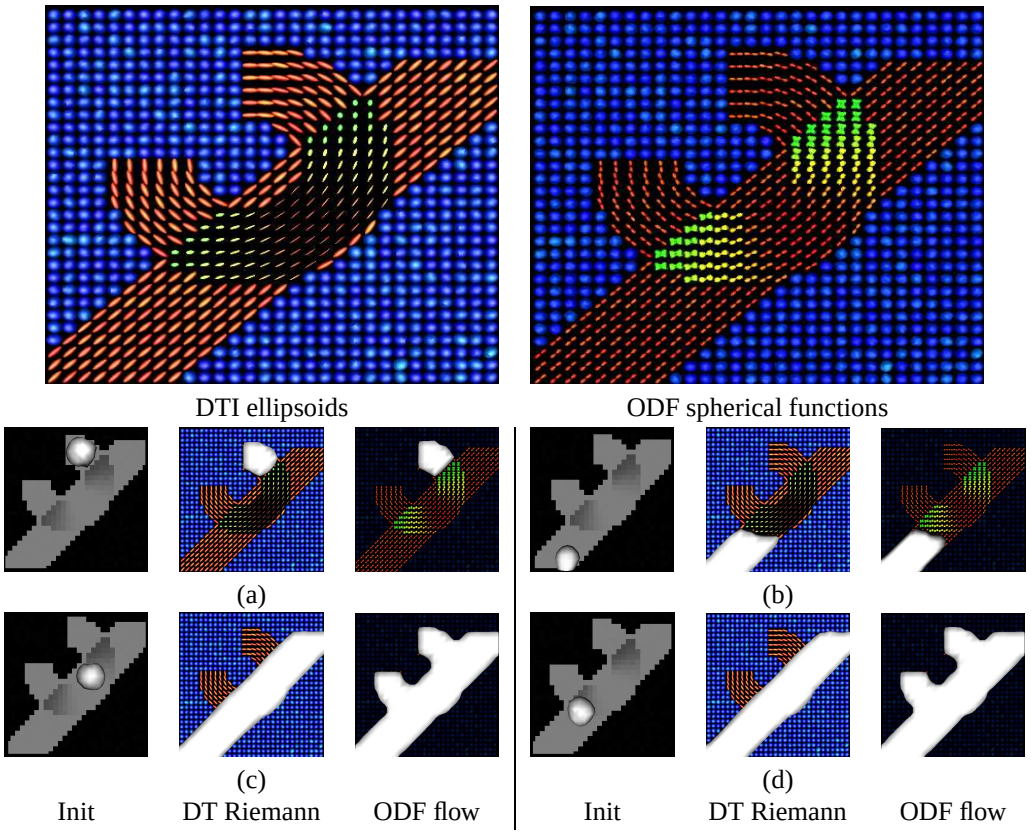

Figure 6: Segmentation on a synthetic 'U'-fiber example. In (a-d), from left to right, the initialization used overlaid on the FA map, the DT Riemannian [24] segmentation and the ODF flow segmentation. The ODF flow is able to propagate through the fiber crossing area and recover the whole structure.

between the ODF flow and DT Riemannian flow can be explained because the crossing region is very small (roughly 3 x 3 x 2 region) and thus, the overall coherence and statistics of the desired structure are not dramatically affected by this crossing. Although the overall shape of the segmentations look the same in Fig. 7, the actual zero level set of the segmenting surface in DT Riemannian and ODF case are slightly different for some voxels at the border the structure, as seen in Fig 8.

4.3 Human Brain Datasets

We have segmentated two large and well-known fiber bundles, the corpus callosum (CC) and the cortico spinal tract (CST), on a human brain with b-value 1000 s/mm^2 and 60 sampling directions

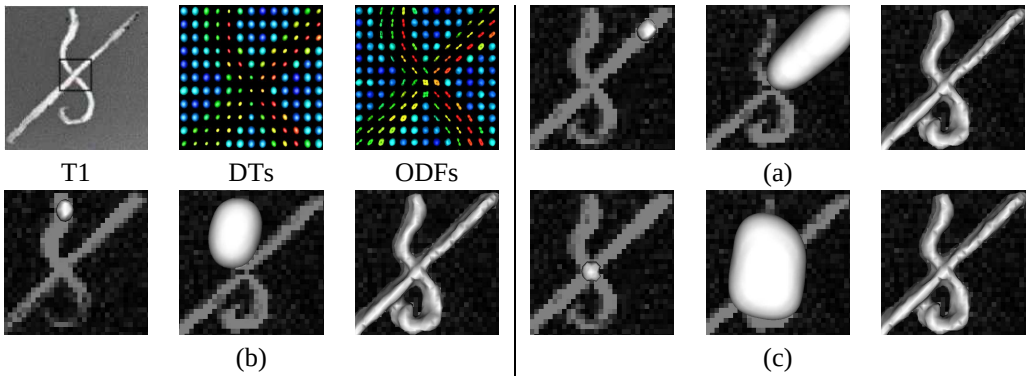

Figure 7: Segmentation on a biological phantom. In (a-c), from left to right, the initialization used overlaid on the FA map, the DT Euclidean [24, 32] flow at $t = 40$ where we see the surface starting to leak outside the fiber structure and the segmentation of the ODF flow.

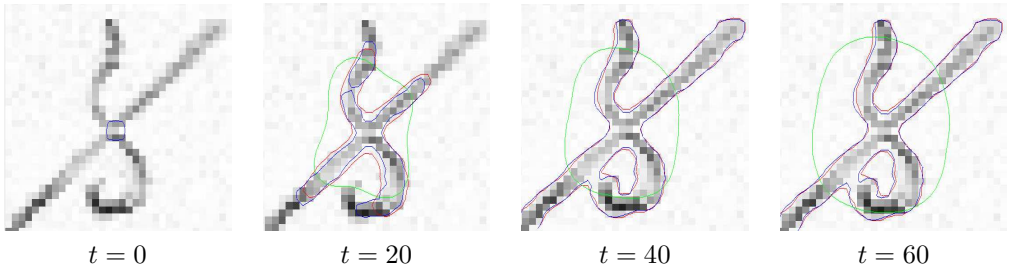

Figure 8: Evolution in time of the zero level set for the DT Euclidean [24, 32] flow (green), DT Riemannian [24] flow (red) and our ODF flow (blue). The contour is placed over the inverted FA map.

and on the database brains with higher b-value 3000 s/mm^2 and 200 sampling directions. Our ODF segmentation on real datasets recovers more structure than other published results on the CC and CST [21, 24, 31, 32, 42]. First, Fig. 9 shows that we are able to reproduce results from [24] with the DT-based flows using both the Euclidean and Riemannian distances. Fig. 9 and Fig. 10 also show that in the DT Euclidean flow, the evolving surface stops near complex crossing area where oblate and isotropic DTs (yellow-greenish DTs) block the flow. The DT Riemannian is able to connect more voxels than the DT Euclidean by slightly evolving into the crossing area. It is interesting to note, in the CST example (Fig. 10), how the flow evolves as to go around complex fiber crossings, i.e. the evolution leaves the expected straight inferior-superior direction to go and pick up the projections of the CC overlapping with the CST and going to project to the superior cortex of the brain. However, in the CST, the flow is still unable to recover the branching fiber structure projecting to the cortex.

The ODF flow recovers that branching structure to the different sulci and also recovers more of the posterior parts of the splenium of the CC.

We also observe that the ODF flow evolves more easily through the crossing area and does so after fewer iterations of the evolution. Convergence is obtained after 100 iterations in the CC and more rapidly after 60 iterations in the CST. It is important to point out that this convergence is obtained automatically without having to heuristically stop the surface evolution at a certain time t. At some point in the evolution, the background (surface $\mathcal{S}_2$) and foreground (evolving surface $\mathcal{S}_1$) statistics stabilize, i.e. the mean and covariance matrix in the two regions become coherent and convergence is attained. Only a few voxels oscillate in and out of the regions $\mathcal{S}_1$ and $\mathcal{S}_2$ on the boundary of the evolving structure.[1] However, as it is often the case in surface evolution algorithms with a boundary term and/or a smoothness term we have to choose a certain value of ν. In the Section 3.3, we have specified our choices of smoothness factor ν. In practice, we observe that for ν too large the evolution stops prematurely and for ν too small the evolution leaks and connects the whole white matter. Fortunately, results are not extremely sensitive to ν and in our experiments, convergence is obtained for ν between 2 and 10 for both synthetic and real data. One still needs to try a few values of ν to obtain the best looking results.

Multi-Subject Study Fig 11 and Fig. 12 show the ODF segmentations for the CC and CST of all subjects of the QBI database [30]. The same parameters were used for all 13 subjects from a single voxel in the medial part of the CC and CST selected (manually) to initialize the flow. It this thus possible to segment the datasets automatically and results are reproducible across many subjects.

Convergence was always obtained automatically for all subjects. Depending on the subject, 80 to 120 iterations of the flow were needed. An iteration takes roughly 0.5 second on a Dell single processor, 3.4 GHz, 2 GB RAM machine. It is thus quite fast to obtain the segmentation for all subjects.

In Fig. 11, we have segmented the complete CC for most subjects with the longer posterior parts of the splenium and the full genu, as in Fig. 9. In the CST example of Fig. 12, we have also obtained segmentation results that are in most cases as complete as the segmentation in Fig. 10. For the CST example, we overlaid the segmented surface on the GFA [34] to clearly see the intended white matter structure to be segmented and also to note the white matter structure differences across subjects. For all subjects, the GFA slice was always the 53^{rd} coronal slice in voxel space.

In both the CC and CST, we note that some evolutions prematurely stopped near the crossing areas for some subjects (e.g. subjects 1, 11 and 13 for the CC and subjects 6 and 7 for the CST). One may think that playing with the segmentation parameters such as initialization and the smoothness ν of the surface might improve and change the results. In fact, in our experiments, this was not the case. A careful visual inspection of the QBI data for these subjects in regions where the flow stops shows two things: 1) Some subjects have "unusual" and "less complete" structures anatomically than others. For instance, subject 13 does not have a curving genu of the CC as all the other subject have. Hence, the CC recovered agrees with the anatomy of subject 13. 2) The ODFs are very isotropic in regions where the flow stops prematurely. The spherical shape of the ODFs are almost

[1] This is seen in the surface evolutions of the CC and CST on the author's web page: http://www-sop.inria.fr/odyssee/team/Maxime.Descoteaux/pages/seg.html

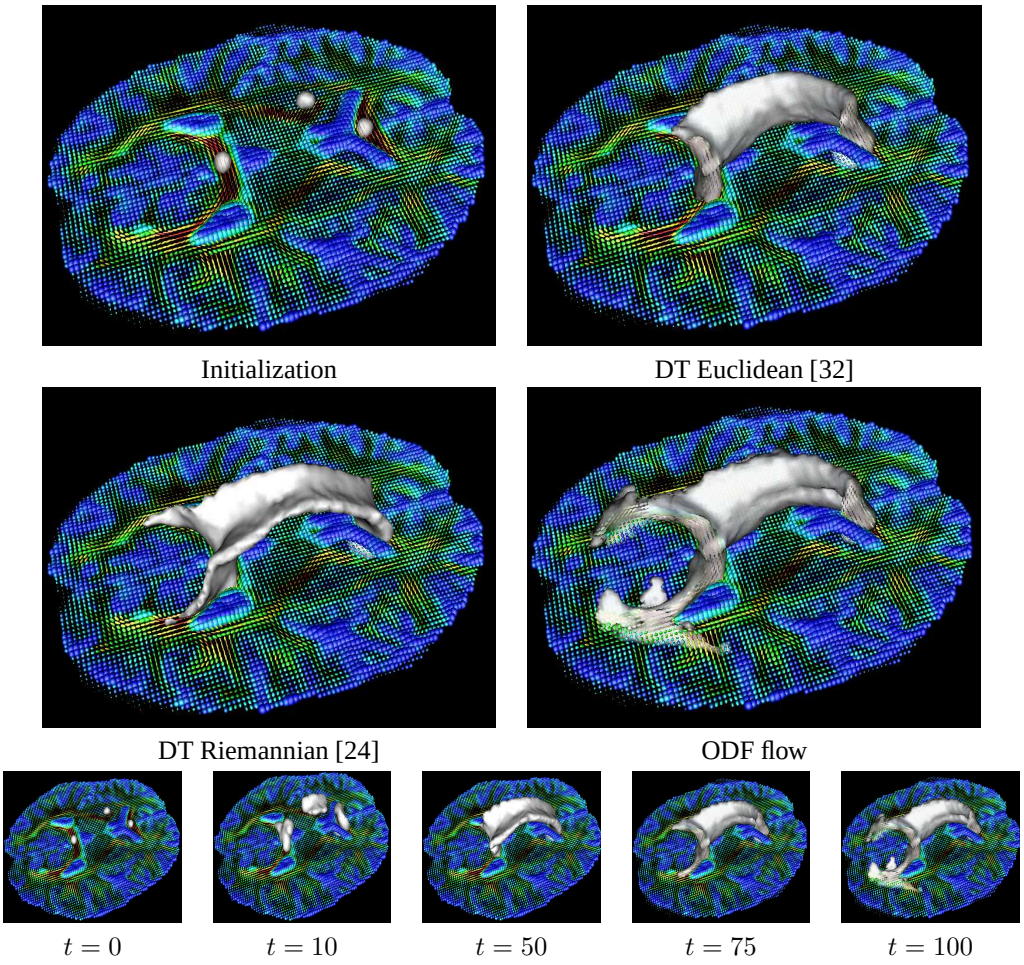

Figure 9: ODF flow segmentations can propagate through crossing regions and get a more accurate segmentation of the corpus callosum (CC). DT-based results from [24] are reproduced. The DT-based segmentations are overlaid on an axial slice with DTs and the ODF flow is overlaid on the same slice with the ODFs. The last row shows the evolution in time of the ODF flow with convergence after 100 iterations.

as isotropic as the DTs. We believe this is because the HARDI signal suffers from major partial signal averaging because of noise due to the high b-value acquisitions and multiple fibers crossing (up to three) in those crossing areas. Hence, there is no coherence between the crossing area and the rest of the desired CC/CST structure to segment. It is thus not surprising that the surface evolution

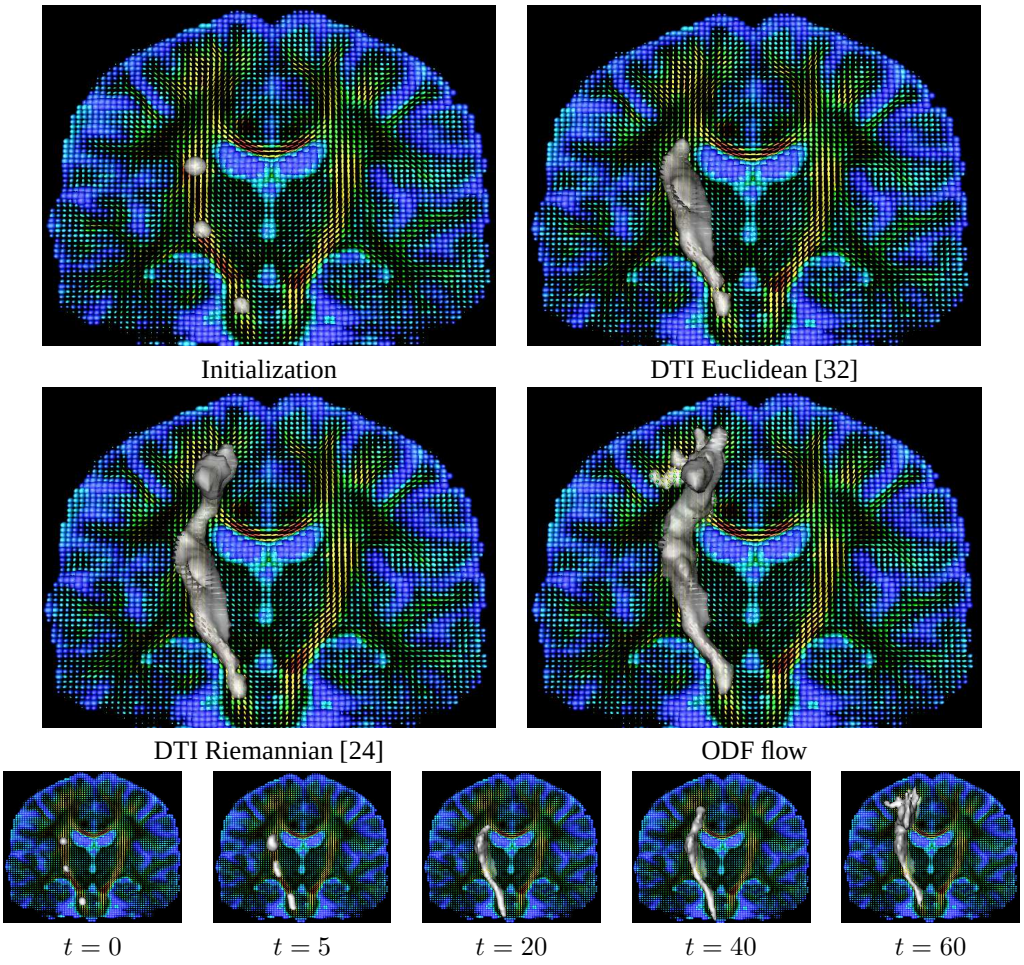

Figure 10: ODF flow can propagate through crossing regions and get a more accurate segmentation of the cortico-spinal tract (CST). DT-based results from [24] are reproduced. The last row shows the evolution in time of the ODF flow with convergence after 60 iterations.

stops. Why does it occur for these subjects and not for the others and why does it not occur for the dataset presented in Figs. 9 and 10? Is it better to have a higher spatial resolution with less angular sampling of the sphere and smaller b-value or a higher angular resolution sampling density with a larger b-value at the cost of larger voxel size and lower SNR?

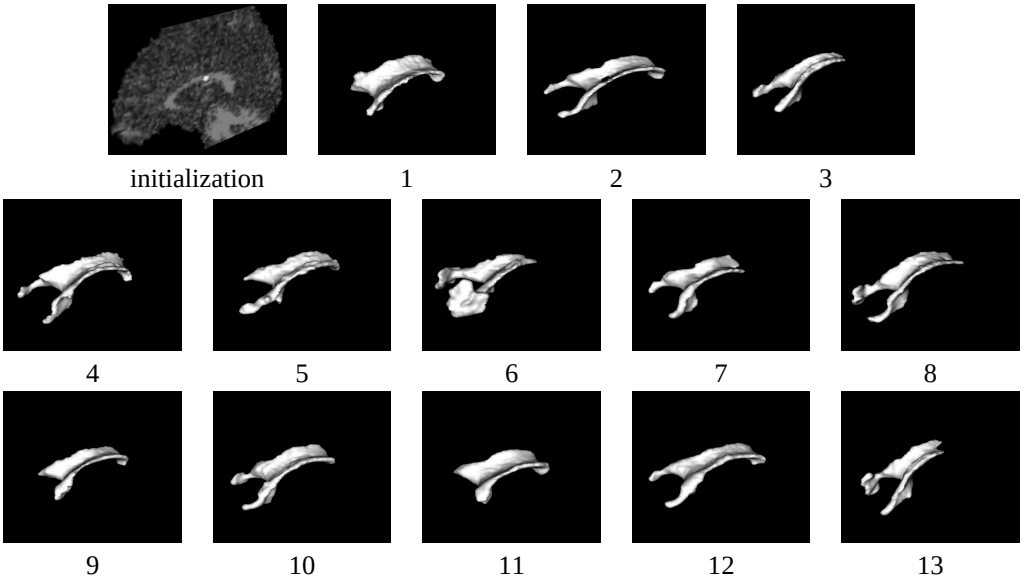

Figure 11: Automatic segmentation of the corpus callosum (CC) using the ODF flow on the 13 subjects of the QBI database [30] from a single seed point in the middle of the CC. Overall CCs are similar and we observe some variability across subjects.

Overall, most CC and CST structures are similar and a significant variability across subject is observed. Hence, it is now important to better understand why these differences occur and propose ways to quantify this multi-subject variability.

5 Discussion

We have presented a unified statistical surface evolution framework for the segmentation of ODF images reconstructed from Q-Ball data. The proposed method combines state-of-the-art HARDI reconstruction and state-of-the-art region-based surface evolution. To do so, we have introduced a similarity measure based on the spherical harmonic description of the ODF. This allowed to formulate a computationally feasible region-based ODF segmentation based on the Euclidean distance between ODF coefficients. Note that this segmentation framework is general and could be used with any input vector of coefficients, for instance coefficients from other HARDI reconstruction methods such as persistent angular structure (PAS) [20], spherical deconvolution [33], or diffusion orientation transform (DOT) [28]. Another contribution of this work was to show how the ODF flow is able to deal with complex fiber configurations such as crossing and branching fibers. In particular, we showed that it is possible to obtain a set of globally coherent ODFs agreeing with well-known

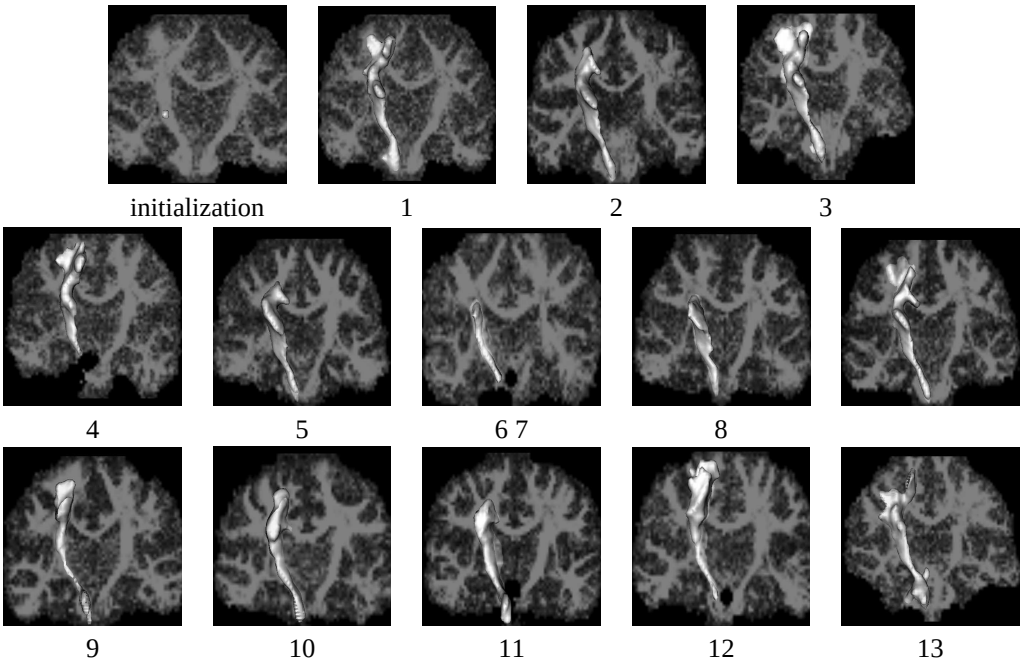

Figure 12: Automatic segmentation of the cortico-spinal tract (CST) using the ODF flow on the 13 subjects of the QBI database [30] from a single seed point in the middle of the CST. For this example, the segmented surface is overlaid on the 53^{rd} coronal slice of the GFA map for all subjects to clearly see the multi-subject variability of the white matter. Overall CSTs are similar and we observe an important variability across subjects.

cerebral anatomical structures. Compared to DTI segmentation, the ODF flow produces more complete segmentations of fiber bundles with crossings. This was illustrated on synthetic datasets, on a biological phantom and on real human brain datasets. Finally, another important contribution was to show the reproducibility of the surface evolution on real datasets with different b-values and angular resolution and also on the 13 subjects from a public QBI database. It is now possible to imagine performing a multi-subject study inside chosen fiber bundles to quantify certain diffusion properties and attempt to follow the evolution of white matter diseases such multiple sclerosis, Parkinson, Alzheimer, etc...

Acknowledgments

We would like to thank M. Rousson and C. Lenglet for their previous work and implementation of the DTI segmentations algorithm with the Euclidean, Kullback-Leibler and Riemannian distances.

We also thank the McConnell Brain Imaging Center and Center for Intelligent Machines of McGill University and especially, J.S.W. Campbell, K. Siddiqi, V. V. Rymar and B.G. Pike for the biological phantom. We are also grateful to to the Max Planck Institute for Human Cognitive and Brain Sciences, Leipzig, Germany and especially, A. Anwander and T. Knoesche for the brain dataset. This exchange was supported by PAI Procope. Thanks also to Cyril Poupon for his help with the QBI database. Finally, this work was partly supported by the diffusion MRI ARC.

A Corollary of the Funk-Hecke Theorem

The FRT at a given spherical point $\mathbf{u}$ is the great circle integral of the signal on the sphere defined by the plane through the origin with normal vector $\mathbf{u}$. This can be written as

$$\mathcal{G}[S](\mathbf{u}) = \int_{|\mathbf{w}|=1} \delta(\mathbf{u}^T\mathbf{w}) S(\mathbf{w}) d\mathbf{w}. \tag{17}$$

To solve this FRT integral involving a Dirac function on the sphere, we first express the signal $\mathbf{S}$ as a spherical harmonic (SH) series of order ℓ and then we need a corollary of the Funk-Hecke theorem [4] to evaluate the integral. The Funk-Hecke formula is a theorem that relates the inner product of any spherical harmonic with the projection on the sphere of any continuous function $f(t)$ defined on the interval $[-1, 1]$. The 3D version is stated in [13, 15]. The proof of the corollary is given in [13, 15] and the corollary is the following:

> **Corollary of the Funk-Hecke Theorem:** Let $\delta(t)$ be the Dirac delta function and Y_ℓ any spherical harmonic of order ℓ. Then, given a unit vector $\mathbf{u}$
>
> $$\int_{|\mathbf{w}|=1} \delta(\mathbf{u}^{\mathrm{T}}\mathbf{w}) Y_\ell(\mathbf{w}) d\mathbf{w} = 2\pi P_\ell(0) Y_\ell(\mathbf{u}), \tag{18}$$
>
> where $P_\ell(0)$ the Legendre polynomial of degree ℓ evaluated at 0,
>
> $$P_\ell(0) = \begin{cases} 0 & \ell \text{ odd} \\ (-1)^{\ell/2} \dfrac{1 \cdot 3 \cdot 5 \cdots (\ell-1)}{2 \cdot 4 \cdot 6 \cdots \ell} & \ell \text{ even} \end{cases} \tag{19}$$

Therefore, the Funk-Hecke theorem and its corollary may be useful for anyone working with SH and seeking solutions to integrals over the sphere.

References

[1] D. Alexander, G. Barker, and S. Arridge. Detection and modeling of non-gaussian apparent diffusion coefficient profiles in human brain data. *Magnetic Resonance in Medicine*, 48(2):331–340, 2002.

[2] D. C. Alexander. Maximum entropy spherical deconvolution for diffusion mri. In *Image Processing in Medical Imaging*, pages 76–87, 2005.

[3] A. Anderson. Measurements of fiber orientation distributions using high angular resolution diffusion imaging. *Magnetic Resonance in Medicine*, 54:1194–1206, 2005.

[4] G. Andrews, R. Askey, and R. Roy. *Special Functions*. Cambridge University Press, 1999.

[5] A. Anwander, M. Tittgemeyer, D. Y. von Cramon, A. D. Friederici, and T. R. Knosche. Connectivity-based parcellation of broca's area. *Cerebral Cortex*, 17(4):816–825, 2007.

[6] P. Basser and C. Pierpaoli. Microstructural and physiological features of tissues elucidated by quantitative diffusion tensor mri. *Journal of Magnetic Resonance*, 111(3):209–219, 1996.

[7] P. T. Callaghan. *Principles of nuclear magnetic resonance microscopy*. Oxford University Press, Oxford, 1993.

[8] J. Campbell, K. Siddiqi, V. Rymar, A. Sadikot, and B. Pike. Flow-based fiber tracking with diffusion tensor q-ball data: Validation and comparison to principal diffusion direction techniques. *NeuroImage*, 27(4):725–736, Oct. 2005.

[9] T. Chan and L. Vese. Active contours without edges. *IEEE Transactions on Image Processing*, 10(2):266–277, Feb. 2001.

[10] D. Cremers, M. Rousson, and R. Deriche. Review of statistical approaches to level set segmentation: Integrating color, texture, motion and shape. *International Journal of Computer Vision*, 72(2):195–215, 2007.

[11] A. Dervieux and F. Thomasset. A finite element method for the simulation of Rayleigh-Taylor instability. *Lecture Notes in Mathematics*, 771:145–159, 1979.

[12] A. Dervieux and F. Thomasset. Multifluid incompressible flows by a finite element method. *Lecture Notes in Physics*, 11:158–163, 1981.

[13] M. Descoteaux, E. Angelino, S. Fitzgibbons, and R. Deriche. A linear and regularized odf estimation algorithm to recover multiple fibers in q-ball imaging. Technical Report 5768, INRIA Sophia Antipolis, Nov. 2005.

[14] M. Descoteaux, E. Angelino, S. Fitzgibbons, and R. Deriche. Apparent diffusion coefficients from high angular resolution diffusion imaging: Estimation and applications. *Magnetic Resonance in Medicine*, 56:395–410, 2006.

[15] M. Descoteaux, E. Angelino, S. Fitzgibbons, and R. Deriche. Regularized, fast, and robust analytical q-ball imaging. *Magnetic Resonance in Medicine*, 2007, to appear.

[16] C. Feddern, J. Weickert, and B. Burgeth. Level-set methods for tensor-valued images. In *Proceedings of the Second IEEE Workshop on Geometric and Level Set Methods in Computer Vision*, pages 65–72, 2003.

[17] L. Frank. Characterization of anisotropy in high angular resolution diffusion-weighted MRI. *Magnetic Resonance in Medicine*, 47(6):1083–1099, 2002.

[18] P. Hansen. The l-curve and its use in the numerical treatment of inverse problems. In *Computational Inverse Problems in Electrocardiology*, pages 119–142, 2001.

[19] C. Hess, P. Mukherjee, E. Han, D. Xu, and D. Vigneron. Q-ball reconstruction of multimodal fiber orientations using the spherical harmonic basis. *Magnetic Resonance in Medicine*, 56:104–117, 2006.

[20] K. M. Jansons and D. C. Alexander. Persistent angular structure: new insights fom diffusion magnetic resonance imaging data. *Inverse Problems*, 19:1031–1046, 2003.

[21] L. Jonasson. *Segmentation of diffusion weighted MRI using the level set framework*. PhD thesis, Ecole Polytechnique federale de Lausanne, 2006.

[22] L. Jonasson, X. Bresson, P. Hagmann, O. Cuisenaire, R. Meuli, and J.-P. Thiran. White matter fiber tract segmentation in dt-mri using geometric flows. *Medical Image Analysis*, 9:223–236, 2005.

[23] L. Jonasson, P. Hagmann, X. Bresson, J.-P. Thiran, and V. J. Wedeen. Representing diffusion mri in 5d for segmentation of white matter tracts with a level set method. In Springer, editor, *Infortation Processing in Medical Imaging*, volume Lecture Notes in Computer Science, pages 311–320, 2005.

[24] C. Lenglet, M. Rousson, and R. Deriche. Dti segmentation by statistical surface evolution. *IEEE Transactions in Medical Imaging*, 25(6):685–700, 2006.

[25] T. McGraw, B. Vemuri, R. Yezierski, and T. Mareci. Segmentation of high angular resolution diffusion mri modeled as a field of von mises-fisher mixtures. In *European Conference on Computer Vision (ECCV)*, volume 3953, pages 463–475, 2006.

[26] S. Osher and J. Sethian. Fronts propagating with curvature-dependent speed: Algorithms based on Hamilton–Jacobi formulations. *Journal of Computational Physics*, 79(1):12–49, 1988.

[27] E. Ozarslan and T. Mareci. Generalized diffusion tensor imaging and analytical relationships between diffusion tensor imaging and high angular resolution imaging. *Magnetic Resonance in Medicine*, 50:955–965, 2003.

[28] E. Ozarslan, T. Shepherd, B. Vemuri, S. Blackband, and T. Mareci. Resolution of complex tissue microarchitecture using the diffusion orientation transform (dot). *NeuroImage*, 31(3):1086–1103, 2006.

[29] N. Paragios and R. Deriche. Geodesic active regions: a new paradigm to deal with frame partition problems in computer vision. *Journal of Visual Communication and Image Representation, Special Issue on Partial Differential Equations in Image Processing, Computer Vision and Computer Graphics*, 13(1/2):249–268, march/june 2002.

[30] C. Poupon, F. Poupon, L. Allirol, and J.-F. Mangin. A database dedicated to anatomo-functional study of human brain connectivity. In *Twelfth Annual Meeting of the Organization for Human Brain Mapping (HBM)*, 2006.

[31] M. Rousson. *Cue Integration and Front Evolution in Image Segmentation*. PhD thesis, Universite de Nice - Sophia Antipolis, 2004.

[32] M. Rousson, C. Lenglet, and R. Deriche. Level set and region based surface propagation for diffusion tensor mri segmentation. In *Computer Vision Approaches to Medical Image Analysis (CVAMIA) and Mathematical Methods in Biomedical Image Analysis (MMBIA) Workshop*, Prague, May 2004.

[33] J.-D. Tournier, F. Calamante, D. Gadian, and A. Connelly. Direct estimation of the fiber orientation density function from diffusion-weighted mri data using spherical deconvolution. *NeuroImage*, 23:1176–1185, 2004.

[34] D. Tuch. Q-ball imaging. *Magnetic Resonance in Medicine*, 52(6):1358–1372, 2004.

[35] D. Tuch, T. Reese, M. Wiegell, N. Makris, J. Belliveau, and V. Wedeen. High angular resolution diffusion imaging reveals intravoxel white matter fiber heterogeneity. *Magn. Res. Med.*, 48(4):577–582, 2002.

[36] L. Vese and T. Chan. A multiphase level set framework for image segmentation using the Mumford and Shah model. *The International Journal of Computer Vision*, 50(3):271–293, 2002.

[37] Z. Wang and B. C. Vemuri. Tensor field segmentation using region based active contour model. In Springer, editor, *European Conference on Computer Vision (ECCV)*, volume Lecture Notes in Computer Science, pages 304–315, 2004.

[38] Z. Wang and B. C. Vemuri. Dti segmentation using an information theoretic tensor dissimilarity measure. *IEEE Transactions in Medical Imaging*, 24(10):1267–1277, 2005.

[39] V. Wedeen, T. G. Reese, D. Tuch, M. Weigel, J.-G. Dou, R. Weiskoff, and D. Chessler. Mapping fiber orientation spectra in cerebral white matter with fourier-transform diffusion mri. In *Proceedings of the International Society for the Magnetic Resonance in Medecine: 8th Scientific Meeting and Exhibition*, number 82, 2000.

[40] M. R. Wiegell, D. S. Tuch, H. B. Larsson, and V. J. Wedeena. Automatic segmentation of thalamic nuclei from diffusion tensor magnetic resonance imaging. *NeuroImage*, 19:391–401, 2003.

[41] H.-K. Zhao, T. Chan, B. Merriman, and S. Osher. A variational level set approach to multiphase motion. *Journal of Computational Physics*, 127(1):179–195, 1996.

[42] L. Zhukov, K. Museth, D. Breen, R. Whitakert, and A. H. Barr. Level set modeling and segmentation of dt-mri brain data. *Journal of Electronic Imaging*, 12:125–133, 2003.

Unité de recherche INRIA Sophia Antipolis
2004, route des Lucioles - BP 93 - 06902 Sophia Antipolis Cedex (France)

Unité de recherche INRIA Futurs : Parc Club Orsay Université - ZAC des Vignes
4, rue Jacques Monod - 91893 ORSAY Cedex (France)
Unité de recherche INRIA Lorraine : LORIA, Technopôle de Nancy-Brabois - Campus scientifi que
615, rue du Jardin Botanique - BP 101 - 54602 Villers-lès-Nancy Cedex (France)
Unité de recherche INRIA Rennes : IRISA, Campus universitaire de Beaulieu - 35042 Rennes Cedex (France)
Unité de recherche INRIA Rhône-Alpes : 655, avenue de l'Europe - 38334 Montbonnot Saint-Ismier (France)
Unité de recherche INRIA Rocquencourt : Domaine de Voluceau - Rocquencourt - BP 105 - 78153 Le Chesnay Cedex (France)

Éditeur
INRIA - Domaine de Voluceau - Rocquencourt, BP 105 - 78153 Le Chesnay Cedex (France)
http://www.inria.fr
ISSN 0249-6399